SUPPRESSION OF DEWETTING IN PULSED LASER MELTING OF THIN METALLIC FILMS ON SILICA

by

James Eric Kline

BS, Washington University in St. Louis, 2000

Submitted to the Graduate Faculty of

School of Engineering in partial fulfillment

of the requirements for the degree

Master of Science

University of Pittsburgh

2005

UNIVERSITY OF PITTSBURGH

SCHOOL OF ENGINEERING

This thesis was presented

by

James Eric Kline

It was defended on

June 28, 2005

and approved by

Dr. John Barnard, Chairman, Department of Materials Science and Engineering

Dr. Jorg Wiezorek, Assistant Professor, Department of Materials Science and Engineering

Dr. Kevin Chen, Assistant Professor, Department of Electrical and Computer Engineering

Thesis Advisor: Dr. John Leonard, Assistant Professor, Materials Science and Engineering

SUPPRESSION OF DEWETTING IN PULSED LASER MELTING OF THIN METALLIC FILMS ON SILICA

James Eric Kline, MS

University of Pittsburgh, 2005

Pulsed excimer laser projection irradiation has been successfully applied to completely melt and resolidify encapsulated elemental metal films of Au, Cu, Cr, and Ni directly on amorphous SiO_2 substrates. A combination of narrow irradiated lines and appropriate SiO_2 capping layers was used to obtain films that do not dewet when fully melted. Detailed processing maps were generated for Au and Ni, while equivalent trends for Cu and Cr were also noted. These systems were analyzed for common behaviors. These behaviors have been generalized into a basic process map that may apply more generally. Experimental parameters and sample preparation criteria are presented to realize such resolidification studies in other metal systems.

TABLE OF CONTENTS

LIST OF TABLES

LIST OF FIGURES

ACKNOWLEDGEMENTS

The author wishes to thank the Department of Materials Science and Engineering at the University of Pittsburgh for providing financial support and facilities for this research. The author wishes to thank Dr. Leonard for his advice and guidance during the last two years.

The author thanks the Penn State Nanofabrication Facility and the Carnegie Mellon Nanofabrication Center for assistance and equipment used in the preparation of samples. Also acknowledged is Dr. Wiezorek for TEM assistance given through the Materials Micro Characterization Laboratory at the University of Pittsburgh.

1.0 INTRODUCTION

Excimer laser irradiation systems are established technology in microelectronics manufacturing where uses span lithography [1], thin film resistor trimming [2], and thin film transistor (TFT) manufacturing (through the super-lateral growth [SLG] technique) [3,4], to name a few. Building on excimer laser acceptance, pulsed laser melting and controlled solidification of thin metal films may become a viable processing route for retention of beneficial local microstructural modifications including, but not limited to, metastable phases and nonequilibrium supersaturations. Before these processing benefits can be attained, the fundamental problem of dewetting (structure formation) and agglomeration ("ball up") of liquid thin films must be overcome. From the microelectronic designer's perspective, dewetting can be viewed as a detrimental film reorganization where an initially flat liquid film develops an undulating surface topology that may contain isolated or continuous holes (ruptures). Because the dewetting process only grows with time, if this dewetting process is not halted, the liquid film will eventually agglomerate into isolated droplets. How this dewetting progresses is of considerable interest in the literature [5-7].

Most liquid metal films on amorphous substrates will dewet upon complete melting [8-10]. The energetic driving force for this dewetting transition is the reduction in high-energy interfacial area between the liquid metal and the substrate. Investigations of pulsed laser melting of thin metal films on SiO_2 have found that dewetting processes can occur on nanosecond timescales [9] but the mechanisms are less clear. The value of this driving force will vary with the residual deposition stresses in the film layers, the interfacial stresses between layers [8], the layer material, and the thicknesses of each layer. As the layer configuration is changed, long-range interactions between the layers [11] may overlap, and so the complete layer stack must be

considered when determining the driving forces. These overlapping contributions diminish when the layer thickness increases above 100 nm [12].

Although a dewetting process can occur via many different progressions, a typical dewetting process is characterized by three broadly defined consecutive steps.

1. Formation and growth of holes
2. Coalescence of holes
3. Formation of islands

Dewetting is in these samples a liquid-phase phenomenon. The metastable solid metal film on SiO_2 will remain continuously attached to the substrate (Section A of Figure 1) until a part of this metal is heated above the melting point. In phase 1, as is illustrated in Section B, the pristine metal surface may develop holes that may be heterogeneously nucleated at defects or irregularities at the upper or lower surfaces of the liquid. Hole creation is a local rupture of the liquid film that exposes a portion of the underlying substrate. Surface tensions tend to minimize the interfacial area between the liquid and the substrate, thereby providing the driving force for continued hole growth. Heterogeneously nucleated holes have fast kinetics and will typically occur significantly before other dewetting mechanisms become active, thereby dominating the apparent morphology if allowed to. Careful sample preparation and judicious selection of the liquid film material are critical if homogeneous or instability-driven holes are to appear.

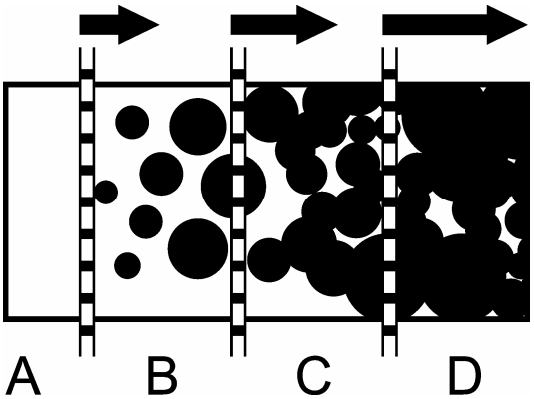

Figure 1: Stages of dewetting progression. Arrows indicate relative melt durations. Black circles represent the relative hole size.

If hole growth is thermodynamically favored, these holes will grow with time. An example of the progression of hole growth is shown in Section B of Figure 1. As hole growth proceeds, eventually these holes will begin to impinge on each other, leading to the start of phase 2, hole coalescence. This coalescence is illustrated in Section C of. As the melt duration extends to longer times, hole coalescence continues. First the liquid metal forms continuous web-like structures. Eventually continued hole coalescence breaks these network connections, and at this point islands of liquid metal form. This island formation is illustrated in Section D of Figure 1.

The dewetting and agglomeration process is in general quite complex. Multiple processes—often competitive—are involved in controlling the final film topology, but these processes can be classified into two distinct phenomena: 1) Nucleation and growth of holes and 2) Dynamic instabilities. For entirely different reasons, each of these processes grows with time and can eventually lead to a rupture, a local exposure of the underlying substrate. A subsequent liquid reorganization of the film can lead to formation of ridges, fingers, and/or droplets. With nanosecond laser melting, nucleation and/or instability-based dewetting processes may be active, depending on the metal-substrate composition, film configuration and preparation, and melt conditions. Often the observed dewetting behavior involves coupling between these mechanisms.

These two phenomena are distinguished by the nucleation and growth process involving a real, and potentially quantifiable critical energy barrier [8]. This nucleation barrier likely is affected by heterogeneities, but the dependence is not known. The dynamic instability process does not involve such an energy barrier and instead involves the multiplication and growth of perturbations with wavelengths in a favorable range. Because these dynamic instability arguments preferably select and amplify a perturbation with a certain wavelength, these arguments parallel the phenomenon of spinodal decomposition. Hence, these instability

arguments are often referred to as “spinodal dewetting.” While this terminology is a misnomer in itself—“spinodal” implies that the second derivative of the free energy curve versus *composition* is negative, not a negative second derivative of the “effective interface potential” with respect to instantaneous layer thickness—these dynamic instability arguments can arise from multiple and unrelated causes, as will be discussed below.

Additional dynamic phenomena may contribute to the metal film losing its continuity and breaking the symmetry of the initially flat semi-infinite film. These phenomena *in elemental metal systems* are as distinct as capillary waves (constant temperature) [13], thermocapillary flow (temperature gradients) [14], and Marangoni forces (surface tension gradients). In earlier experiments [15,16], surface “ripples” of similar periodicity (1-5 μm) and morphology have been shown to arise from non-uniform or tilted irradiation at the target surface. These “ripples” resulted from complicated non-linear optical effects at the surface of the target, and will be of particular concern with highly coherent solid-state Ruby or YAG systems that have complex mode structures and speckle contrast. The above phenomena create a topology on the surface of a liquid metal created by melting the solid metal underneath. Causes aside, these dynamic surface features grow in amplitude with increasing melt duration.

Alternatively, changing the sample configuration to include a solid layer resting upon a liquid can significantly change the stability of the liquid layer [17] with respect to dewetting. This approach was successfully applied to SiO_2-encapsulated Si, thereby allowing the laser processing that is now used in the fabrication of TFT monitors [18]. In a different approach, if the substrate surface is considered viscous and not rigid, the kinetics of a growing hole are retarded [19].

2.0 SAMPLE FILM PREPARATION

Samples were prepared via sputter deposition of elemental nickel and gold films on thermally oxidized (1 μm) Si (001) wafers. Before deposition, the SiO_2 substrate surface was rinsed with acetone, isopropanol, and then deionized water; the substrate was blown dry with canned dry air (Cr and Ni samples) or with nitrogen gas (Cu and Au). The substrates were not wiped dry in any case, so not to add to the native SiO_2 roughness or to abrade patterns in the substrate before deposition[20]. This lack of contact drying should eliminate any systemic substrate surface roughening that can act as preferred nuclei sites for film rupture. Pre-sputtering of the SiO_2 substrate surface was not attempted in any of the experiments.

The sample configuration for each different metal system is illustrated in Figure 2. Samples with 200 nm Ni films were prepared by magnetron sputtering unheated in an Innovative Systems ISE-OE-PVD-3000 under a base pressure of approximately 6.7×10^{-4} Pa (5×10^{-6} Torr), working pressure of 0.67 Pa (5 mTorr) Ar, and 100 W target power. In a class 100 clean room, 580 nm of SiO_2 was later deposited in a Perkin-Elmer 2400-8L RF system under a base pressure approximately 6.7×10^{-5} Pa (5×10^{-7} Torr, passive heating, 5 mTorr Ar working pressure. Voltages were 200 W forward (4 W reflected), 3 V substrate bias, 810 V to target, and the deposition rate was 2.57 nm/min. Samples with 200 nm Au films were prepared in the same class 100 clean room by magnetron sputtering in a Perkin-Elmer 2400-6J under a base pressure of 1.1×10^{-4} Pa (8×10^{-7} Torr), working pressure of 0.67 Pa (5 mTorr) Ar, room temperature, and 50 W target power. The Au samples were immediately transferred to the same Perkin-Elmer 2400-8L RF system for the SiO_2 deposition under conditions identical to the Ni encapsulation above. Sample films of 200 nm Cu were deposited by magnetron sputtering in a CVC Connexion Sputtering System under a base pressure of approximately 2×10^{-8} Torr, working pressure of 5

mTorr Ar, room temperature, 150 W target power. The Cu samples were immediately transferred to the same Perkin-Elmer 2400-8L RF system for the SiO_2 deposition under conditions identical to the Ni encapsulation above.

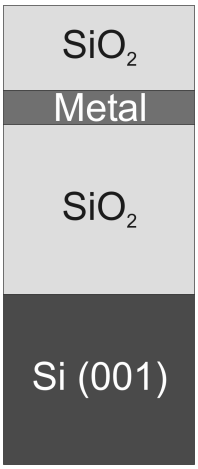

Figure 2: Typical layer configuration. The capping SiO_2 is 580 nm thick and is RF magnetron sputtered. The metal layer consists of 200 nm Au, Cu, or Ni and is magnetron sputtered. The substrate is Si (001) with 1 μm thermally grown SiO_2.

For Cr, 200 nm of metal film was sputter deposited on Si (001) wafers with 1 μm thermal SiO_2. These samples where capped with 500 nm of plasma enhanced chemical vapor deposited (PECVD) oxide using a Plasma Therm ECR-PECVD system under a working pressure of 4 mTorr, 900W microwave input, 100^{o}C substrate temperature; and flow rates of 5.1 sccm CF_4/O_2, 3 sccm Ar, and 4 sccm SiH_4 to produce a deposition rate of 10.7 nm/min.

3.0 ILLUMINATION SYSTEM

The projection illumination system, as shown in Figure 3, consisted of a Lambda Physik EMG-202 KrF excimer laser operating at 248 nm with a full-width-half-maximum pulse duration of 25 ns, a collimating telescope, energy meter, a stainless steel or copper single-slit mask, and a single fused silica lens positioned for a 5x demagnification. The mask was adjusted for projection of narrow lines, 3 μm or larger, on the sample.

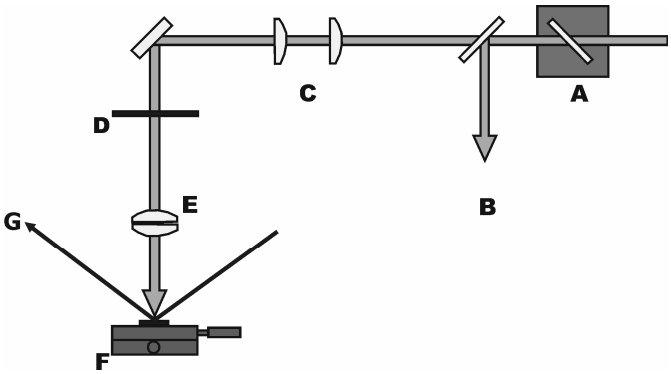

Figure 3: The 5x demagnification illumination system used in the pulsed laser melting experiments. A) variable attenuator, B) energy meter, C) conditioning telescope, D) copper mask, E) imaging lens, F) translation stage, G) TR system for Si surface melting calibration.

The excimer laser fluence, incident energy per square centimeter [J/cm^2], was calibrated to the surface melting of bulk Si (001) under flood irradiation. Standard surface reflectance measurements of the melt duration were compared to 1D numerical simulation [21][i], which predicted a surface melt threshold of 675 mJ/cm^2 given the measured pulse temporal profile. The overall fluence calibration extended from 25 mJ/cm^2 to 2.5 J/cm^2.

Beam profiles were analyzed by observing the image pattern on a 50 nm LPCVD SiO_2/50 nm LPCVD a-Si/100 nm thermal SiO_2/Si (001) wafer that undergoes striking color changes for the

[i] The 3DNS simulation program is described in Section 4.0 below.

fluence onset thresholds of surface melting and full melting, respectively. This imaging wafer provided a second calibration source for fluences down to 100 mJ/cm^2. The illuminated transverse profile closely approximates a step function profile for line widths above 10 μm; line widths below 10 μm approach a Gaussian intensity profile with decreasing maximum amplitude. The spatial coherence was typically 2.0 microns or better, as estimated from the sharpness at the edges of the line. There was negligible variation in fluence in the longitudinal direction along the line for the areas examined.

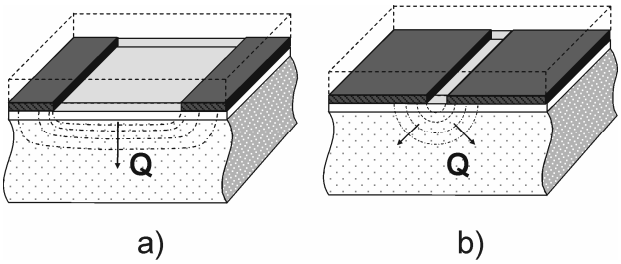

Figure 4: Schematic of line illumination in these experiments. The edges of the capping layers are drawn in dotted line. The liquid metal pool is represented as the lighter blocks. a) Wide line irradiation. b) Narrow line irradiation

For low fluences, the metal layer is heated to temperatures not exceeding the surface melting threshold of the metal. The heat generated during illumination is withdrawn by conduction vertically into the substrate. For slightly higher fluences, the surface of the metal is heated above the melting point, but the melt depth does not penetrate the full depth of the metal film. Here some residual crystallographic material from the as-deposited film is retained during partial melting. The partial melting threshold corresponding to all line widths in which the heat flow is predominantly one-dimensional, as in Figure 4a, is a constant value. As the heat flow becomes increasingly two-dimensional for small line widths as in Figure 4b, the partial melting threshold is expected to rise somewhat.

Fluences substantially higher than the partial melting threshold result in complete melting of the metal film. Due to the complex competitive nucleation and growth processes in this regime, the completely melted metal and its resolidified microstructure is expected to differ from the as-deposited state and will vary as the processing conditions are changed.

4.0 SIMULATIONS

The 3DNS simulation package was used to simulate the laser melting and resolidification conditions in these experiments, as well as calibration to silicon surface melting. The 3DNS program models the laser interactions with matter, the resultant heat flow, phase change, and nucleation information with nanosecond resolution and three-dimensional, nanometer spatial resolution. It does this by a finite differences algorithm that uses inputs of a scaled temporal excimer laser pulse trace, material property files, and configuration parameter files. The simulation package can report the solid-liquid interface motion; its temperature, velocity, and direction; and nucleation histories when properly configured. The excimer laser pulse is recorded with a storage oscilloscope and then scaled to the appropriate maximum energy. The material files contain detailed optical, thermophysical, and kinetics information for each material in use. Simulation parameter files are used to select reported information, to enable/disable kinetic processes (i.e. no nucleation, no melting, etc.), and to reproduce the sample's geometry. Like any simulation, care must be taken to ensure that the simulation reproduces physical events. Once the material files are compiled from available reference data, the simulation parameter file is initially run with a minimum of complexity. In practice, one often adapts a prior simulation to the current sample configuration. By starting with a functional simulation, stability, accuracy, and reproducibility concerns may be addressed. Incremental changes are made to the simulation before it is run; this process is iteratively repeated until all parameters have been adapted and the results converge upon a single pathway.

Simulation results are reported as simple ASCII text files, so these text files must be analyzed in a standard mathematical computing program. The current version (v3.9) uses Mathematica®

V4.2 as the analysis and plotting program. The use of Mathematica allows some small degree of automation, especially when running multiple simulations where only one parameter is varied.

While the simulation package was used to calibrate the excimer laser fluence at the sample surface, this calibration procedure will not be reproduced here. Melting and resolidification simulations were performed for capped and uncapped Au and Ni films. Simulations involving Cu were attempted, but the similarities between Au and Cu did not justify the additional work to hone initial estimates. The simulations of uncapped Au and Ni produced threshold numerical values favorable to the experimental data. The specific thermophysical parameters for Au, Ni, and SiO_2 used in these simulations are presented below in Table 1. Building upon this, simulations of capped Au and Ni were attempted. These simulations, however, did not agree with experimental data as well. Relative values of partial and complete melting scale reasonably well to experiment, but the absolute values are rather different. This scaling is expected given the uncertainty associated with thin film absorption/reflection effect during melting and the different heat flow considerations. The capping layer will act as a heat sink/source at different times in the experiment, but these effects are not well-understood.

Table 1: Simulation parameters for SiO_2, Au, and Ni.

	SiO_2	Solid Gold	Liquid Gold
Melting Temperature [K]	–	1337	
Heat of Fusion [J / cm^3]	–	1252.25	
Optical Index (248 nm)	1.515 + 0***j***	1.484 + 1.636***j***	1.582 + 1.988***j***
Heat Capacity [J / (cm^3 K)]	2.7516 + (4.9850e-4)T – (1.0032e5) / T^2	6.5529 – 21.5423 / $T^{0.5}$ – 0.7779$T^{0.25}$ + (1.433e-3)T	2.87
Thermal Conductivity [W / (cm K)]	0.0134	4.3614 + 25.6885 / $T^{0.5}$ – 10.9827 / $T^{0.25}$ – (4.3460e-7)T^2	2.4
Interface Response Function [m/s]	–	1.196(T – 1337)	–

	Solid Nickel	Liquid Nickel
Melting Temperature [K]	1726	
Heat of Fusion [J / cm^3]	2652.25	
Optical Index (248 nm)	1.40 + 2.10***j***	2.01 + 3.25***j***
Heat Capacity [J / (cm^3 K)]	T < 591.5 4.07868 – (2.63607e-3)T + (7.66345e-6)T^2 1726 > T > 591.5 -8.38555 + (5.28746e-2) / T^3 + 19.7561 / T^2 + 4746.75 / T + (1.10207e-2)T – (2.73932e-6)T^2	5.84
Thermal Conductivity [W / (cm K)]	0.198275 + 149.981 / T + (3.87276e-4)T + (7.09543e-8)T^2 – (8.11100e-11)T^3	2 + (4.03352e-2)T + (3.14634e-4)T^2 – (2.89377e-8)T^3
Interface Response Function [m/s]	1.0(T – 1726)	–

5.0 FLOOD IRRADIATION OF UNCAPPED FILMS

In the first set of experiments, samples of uncapped Ni, Au, Cu, and Cr films were irradiated by single excimer pulses over a wide range of fluences. Upon complete melting, in which the pulse melts the entire film down to the underlying SiO_2, dewetting was experimentally observed in all cases for 100 and 200 nm Au and Ni films as shown in Figure 5. For Ni, the dewetting process was found to occur by a progression from isolated hole formation to hole coalescence, and then to island formation with increasing fluence. An example is shown in Figure 5a. For gold, the dewetting behavior with increasing fluence was somewhat different, as shown in Figure 5b. Dewetting occurred with a progression from a few widely spaced holes to holes with connecting tears to isolated irregular islands, to droplet formation and film removal. In all cases, the experimentally observed complete melting thresholds of 500 mJ/cm^2 for Ni and 130 mJ/cm^2 were in good agreement with 1D numerical [21] simulations that predicted 500 mJ/cm^2 and 170 mJ/cm^2 for 200 nm uncapped Ni and Au films, respectively. At lower energies corresponding to the partial melting regime, the films remained continuous, but with some surface roughening.

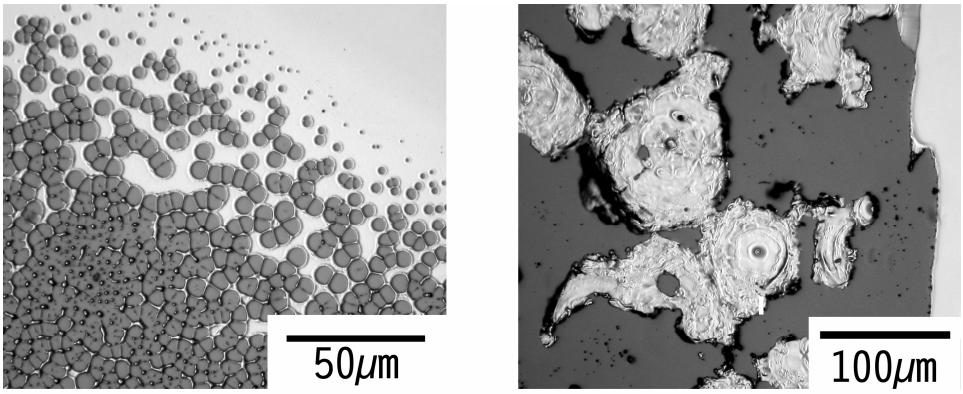

Figure 5: Reflection micrographs of film morphologies for uncapped films after flood irradiation a) Ni 100 nm on 1 μm thermal oxide at 500 mJ/cm^2, and b) Au 100 nm on 1 μm thermal oxide at 80 mJ/cm^2

Pattern analysis to determine the nature of the dewetting events [22] (nucleation vs. instability arguments) was not attempted; regardless of origin, the liquid films dewet during the laser processing.

For these uncapped films, the series of flood illumination observations over a range of fluences revealed the progression from non-melting through the partial melting and complete melting thresholds. The partial melting threshold was attributed to an onset of a sudden change in color and apparent metal surface roughening. This surface roughening and color change becomes increasingly pronounced as the fluence is raised. At a certain point, however, the surface of the metal becomes disturbed by a series of dewetting events. Because dewetting events can only occur in the completely melted regime, the complete melting threshold was determined by the lowest fluence where identifiable dewetting events occur.

6.0 MELT THRESHOLDS IN CAPPED FILMS

Identification of suppressed dewetting behavior in the capped Ni and Au films depends critically on careful fluence calibrations and determination of partial and complete melting thresholds. Effects that must be considered include: 1) The addition of a capping layer may change the reflectivity of the sample, act as a heat sink, or possibly change the visual appearance of the thresholds that were identified in the uncapped films. 2) Limitations of the optical projection system reduce the beam throughput and change the intensity profile transverse to the line for line widths below 12 μm. Additionally, it is recognized that illumination of narrow lines can lead to enhanced two-dimensional heat flow [23], but only for line widths below 2 μm.

Single shot flood illuminations (>500 μm spot size) were performed on Au and Ni films beneath a 580 nm capping SiO_2 layer, over a large range of fluences (typically 25-1000 mJ/cm^2) as shown in Figure 6. The characteristic surface morphologies of the solidified films were found to vary with increasing fluence and to reveal partial and complete melting behavior similar to the uncapped films. Here, two melting regimes can be easily identified: Partial melting (PM), in which the upper portions of the metal film have been melted and a color change or roughness appears; and Complete melting (CM) where the film has been fully melted down to the underlying SiO_2. In these flood illuminations of capped Ni films, the liquid metal dewets upon complete melting. In Au, the CM threshold is the fluence at which the metal film transitions from the roughened morphology of PM into a much smoother surface morphology with a characteristic uniform luster, and may include isolated dewetting events.

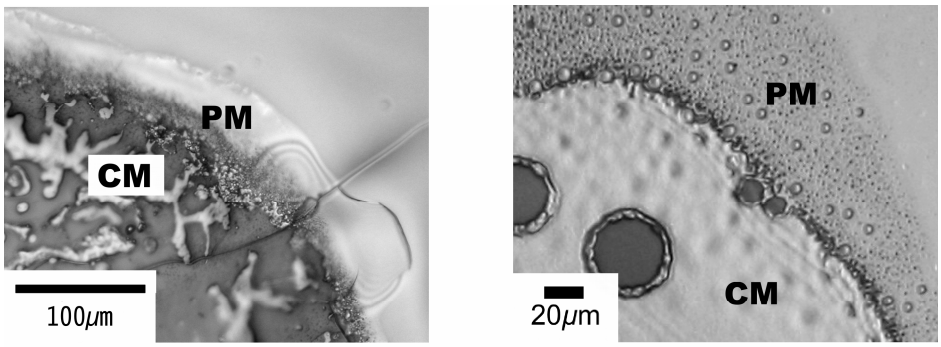

Figure 6: Film morphologies for each fluence regime a) Edge of flood irradiation at 555 mJ/cm^2 at center on Ni. b) Edge of flood irradiation of 535 mJ/cm^2 at center on Au. Regions include partial melting (PM) and complete melting (CM).

The melt thresholds for capped Au and Ni films were experimentally determined for Ni at 150 mJ/cm^2 and 300 mJ/cm^2 for partial melting and complete melting, respectively; and for Au at 200 mJ/cm^2 and 425 mJ/cm^2 for partial melting and complete melting, respectively. These observations were compared to one-dimensional simulations of melting and resolidification of uncapped and capped Au and Ni thin films were performed using the 3DNS simulation package as described in Section 4.0 above. Simulations were used to substantiate observations, and indicated partial and complete melting thresholds of (185 and 240 mJ/cm^2) for Au and (360 and 545 mJ/cm^2) and Ni films. Agreement is believed to be reasonable given the uncertainties associated with thin film interference effects.

7.0 MICROSCOPY

Post-illumination observations were performed primarily via optical microscopy (including differential interference contrast microscopy) and later via TEM analysis. TEM was used to verify optical observations of complete melting of Au, Cr, and Cu by noting an abrupt change in the laser modified microstructure in the irradiated line at a critical fluence threshold. While the laser modified microstructure in Ni was not significantly different from that of the as-deposited film, the complete melting threshold was inferred from analogy of similar morphological evolutions in Cr and the absolute fluence values (at once line width).

TEM sample preparation was performed by a simple lift-off procedure involving 49% HF and a rinse in DI water (Au) or pure ethanol (Cu, to prevent oxidization). At 200 nm thickness, the Au films are only partially electron transparent (at 200kV accelerating voltage) and hence required a 25% thinning in diluted aqua regia before examination. TEM samples of Cr were prepared by a back-etch of the silicon wafer followed by HF immersion to remove the encapsulating SiO_2.

8.0 EXPERIMENTAL RESULTS

For the systems Au and Ni, there is a practical limit to the encapsulation technique in that the process window for suppressed dewetting is a function of line width. As noted in Figure 5, the process window for Ni is found to close abruptly at a line width between 33 and 40 μm. Subsequent experiments on Au indicated that the process window in Figure 5b for Au extends in some form to 90 μm, but continues to narrow with increasing line width. At flood illumination, the process window for Au, if it exists, was not positively identified.

8.1 LINE IRRADIATION OF CAPPED NI AND AU FILMS

In a series of experiments, Ni and Au metal films were capped by 580 nm of sputtered SiO_2 and irradiated with single excimer pulses projected as narrow lines of adjustable width. In all cases the metal film thickness was 200 nm, and the SiO_2 capping layer was 580 nm, deposited at low temperatures and rates as described above to reduce stress. After melting and resolidification, the irradiated regions were examined by optical microscopy, with examples shown in Figure 7 and Figure 8. Detailed analysis of the beam intensity profile, numerical simulation, and the calibration procedure described above were used to determine the fluence in the projected line. The smooth morphology in the center of each line corresponds to complete melting. Additionally, the occasional appearance of isolated round holes, possibly at defects, was observed in these central regions—confirming that the film had been fully melted.

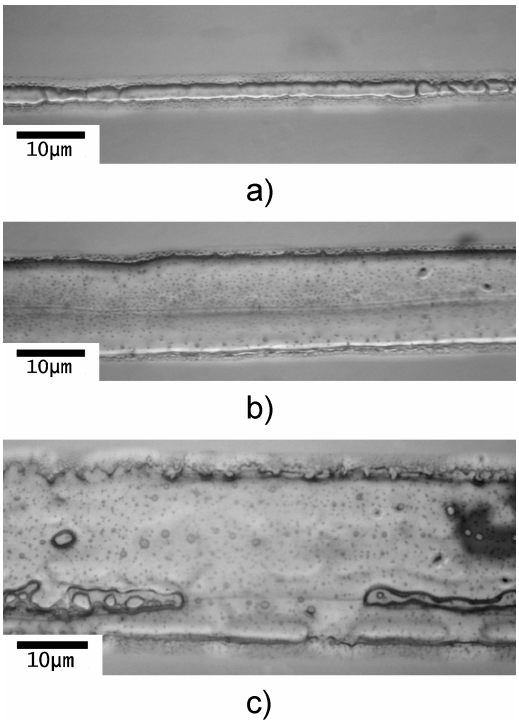

Figure 7: Reflection micrographs of line irradiations of capped 200 nm Ni films at a) 5 µm line width, 590 mJ/cm^2, b) 16 µm line width, 600 mJ/cm^2, c) 33 µm line width, 345 mJ/cm^2.

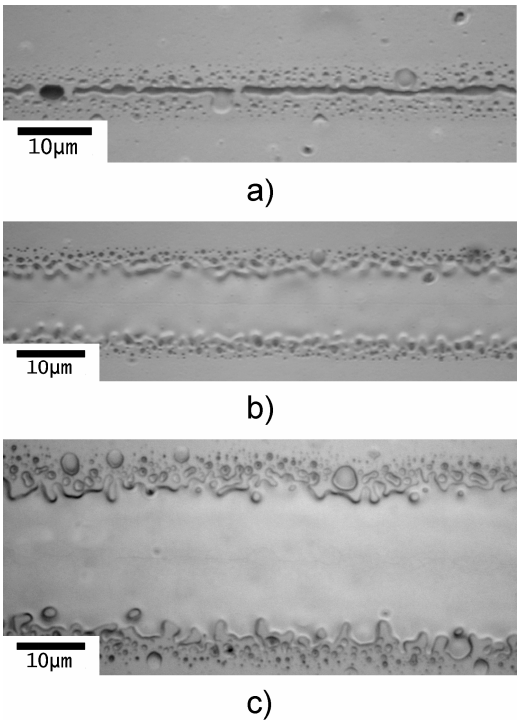

Figure 8: Reflection micrographs of line irradiations of capped 200 nm Au films at a) 6 µm line width, 600 mJ/cm^2, b) 16 µm line width, 430 mJ/cm^2, c) 30 µm line width, 470 mJ/cm^2.

Through a series of tests at various line widths and fluences, a process window was found in which films were completely melted but remained continuous throughout the melting and resolidification process. The results are summarized in the maps of Figure 9. In the case of capped Ni, dewetting was fully suppressed in a band of fluence values immediately above the complete melting threshold, as shown in Figure 9. At higher fluences, some isolated dewetting was observed in the laser-melted region, typically associated with cracks in the capping SiO_2 layer as seen in Figure 7c. At the highest fluences, the SiO_2 cap was significantly damaged or removed, and the film fully dewet. For lines wider than 33 μm, damage to the SiO_2 cap and dewetting of the Ni film were found for all fluences above the complete melting threshold.

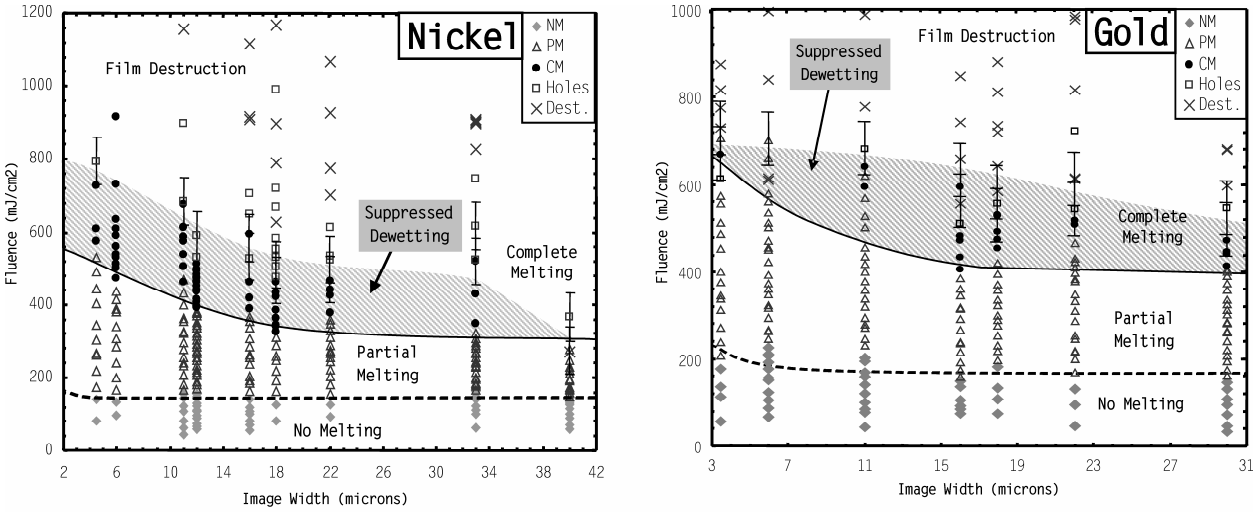

Figure 9: Maps of observed film morphology after solidification for encapsulated 200 nm a) Ni and b) Au films. Shaded regions indicate complete melting and resolidification of the metal film while maintaining continuity (suppressed dewetting).

With Au films dewetting was also fully suppressed above the complete melting threshold, but in a narrower range of fluences, as shown in Figure 9b. Here films remained continuous in lines up to 30 μm wide, with very smooth post solidification morphology. Damage to the SiO_2 capping layer at higher fluences was less obvious, with holes and full dewetting of the Au film

occurring beneath the SiO_2 cap, which remained intact with no visible cracks. At the narrowest line widths, as in Figure 8a, the completely melted area is quite narrow and is flanked by wide areas corresponding to partial melting. This is due to optical limitations that result in a nearly Gaussian transverse intensity profile.

8.2 LINE IRRADIATION OF CAPPED CU AND CR FILMS

There are preliminary indications that the processing window for Cu is much larger than for Au, but this process window has not been mapped out. The process window for Cu likely could be extended to flood illumination with a more exacting study of the interfacial energies as a function of temperature. Optical microscopy of irradiated lines in Cu (Figure 10a) revealed little information, as the irradiated areas display very little contrast from the as-deposited film. Initial TEM analyses for approximately 90 μm and fluence of 850 mJ/cm^2 lines revealed that the metal film was indeed completely melted. It has also been observed that flood illumination of Cu does not initiate dewetting until fluences of approximately 1.0 J/cm^2, a fluence at which film damage is likely to occur.

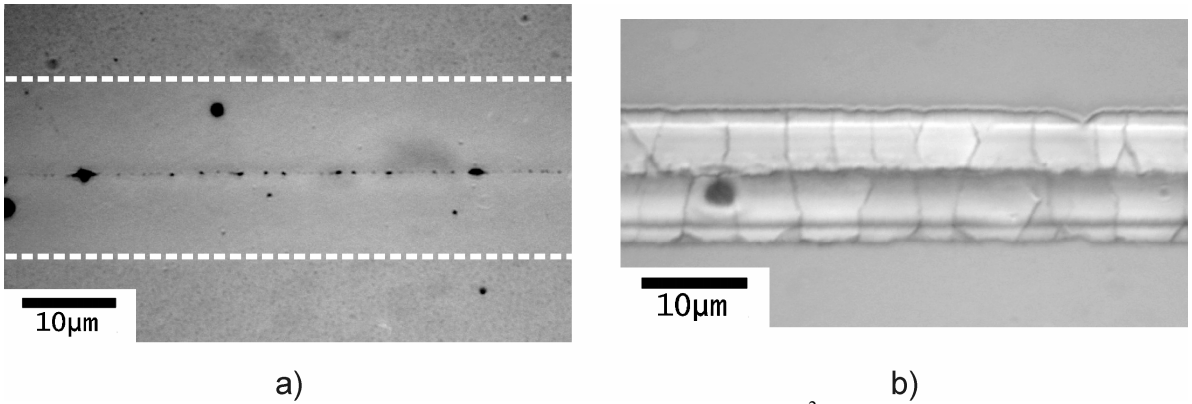

Figure 10: Optical micrographs of suppressed dewetting. (a) Cu at 850 mJ/cm^2, contrast strongly enhanced, dotted lines show melt edges; and (b) Cr at 600 mJ/cm^2

Preliminary indications for Cr suggest a processing window similar to that of Ni, but this process window has not been mapped out. An optical micrograph of line melting of Cr is presented in Figure 10b. Initial TEM analysis of 9 μm line widths under 500 mJ/cm^2 reveal the film was completely melted. Tears in the metal film are likely associated with post-solidification thermal stresses.

9.0 DISCUSSION

As mentioned in the introduction to this thesis, the dewetting process is the process of structure formation when the substrate is exposed through liquid motion driven by reduction of high-energy interfacial area between the liquid and the substrate. The actual dewetting process will depend on materials and their layer thicknesses, but dewetting usually occurs by some combination of nucleated holes and instability-driven film rupture. The sections that follow discuss the changes in energetics and thermodynamics of the system when a capping layer is added.

9.1 SURFACE ENERGY EFFECTS

The addition of a capping layer can have a significant effect on the energetics and dynamics of the thin liquid film dewetting process [17,24]. The current experiments indicate that Ni, Au, Cu, and Cr films that normally dewet upon laser melting remain continuous when capped with a 500+ nm SiO_2 thick film [25]. Although these observations do not reveal which specific dewetting processes are active or dominant, it is clear that the presence of capping layer is suppressing or slowing the mechanisms associated with dewetting as observed in uncapped films. For this reason, it is useful to consider how the presence of the cap can affect the thermodynamics and kinetics of this system.

Uncapped thin films of molten metals such as Ni, Cu, or Au on SiO_2 substrates are unstable with respect to dewetting. The spreading parameter for an uncapped film is given in [EQN 001]

$$S = \gamma_{sg} - \left(\gamma_{ls} + \gamma_{\mathrm{lg}}\right) \quad \text{[EQN 001]}$$

where the γ_{sg}, γ_{ls}, and γ_{lg} are the solid-gas, liquid-solid, and liquid-gas interfacial energies,

respectively. When the spreading parameter is negative, the Gibbs free energy of the system is lowered by liquid agglomeration that leads to uncovering of the solid substrate. A balance of these stresses for an equilibrium liquid island shape on a thick, homogeneous substrate is related to an equilibrium contact angle through Young's equation [EQN 002].

$$\gamma_{sg} - \gamma_{ls} = \gamma_{lg} \cos\theta \quad \text{[EQN 002]}$$

A critical rupture in a capped liquid film can occur in two ways, as shown schematically in Figure 11. In the first case, the liquid film remains attached to the encapsulating oxide. This geometry can result from 1) viscoelastic motion leading to nucleation of isolated regions of thinning, 2) dynamic undulations in the upper liquid-solid interface, or 3) mechanical buckling of the capping layer. There is a positive energy associated with the perturbation that involves an increase in the increased liquid-solid interfacial area, as well as viscous motion in the liquid and capping layer. The dynamics will be strongly determined by the viscoelastic properties of the capping layer, which in the case of SiO_2 is calculated to be 2.9 x 10^{13}, and 3.9 x 10^{8} (Pa•sec) at the respective metal melting temperatures (1337 K for Au, 1726 K for Ni). It drops to 78.9 and 28.8 (Pa•sec) at their respective boiling temperatures (2983 K for Au, 3186 K for Ni).

Rippling of SiO_2 capping layers up to 200 nm thick on pulsed laser-melted Si has been observed [26,27], but is believed to be due to the relief of stress due to thermal expansion during melting or stresses introduced during deposition—and not due to film dewetting processes. Numerical simulations for the current experimental conditions show that the maximum temperatures are reached only near the capping SiO_2-liquid metal interface, while the surface of the 580 nm cap remains near ambient temperature. This suggests that the through thickness of SiO_2 cap in the current experiments is sufficiently rigid to prevent rippling of the liquid layer on nanosecond timescales.

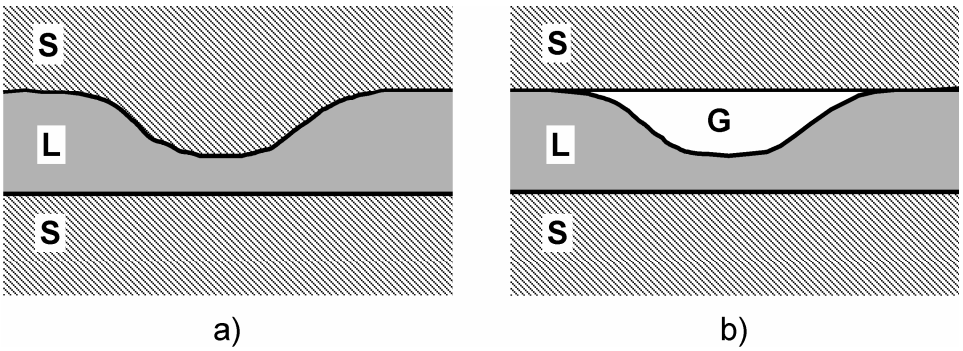

Figure 11: Possible geometries for initiation of dewetting in SiO_2 -capped molten metal films. a) Thinning of film via viscoelastic motion or buckling of the capping layer. b) Gas-filled void formation at upper liquid-solid interface.

In the second case, shown in Figure 11b, a liquid film perturbation may involve separation from the capping layer. Whether arising via a nucleation and growth or via dynamic fluctuations, it is possible to calculate the net energy difference relative to uncapped films [8]. For an uncapped film, a perturbation involves a net positive energy associated with an increase in the area of the liquid free surface,

$$\Delta E_u = \gamma_{lg} a_h - \gamma_{lg} a_1 \quad \text{[EQN 003]}$$

where a_h is the new area of the perturbation, and a_1 is the area of the original undisturbed surface. In the presence of a capping layer (identical in composition to the substrate), the net energy becomes

$$\Delta E_c = \gamma_{lg} a_h + \gamma_{sg} a_1 - \gamma_{ls} a_1 \quad \text{[EQN 004]}$$

Combining [EQN 003] and [EQN 004], and the use of Young's relation [EQN 002] yields an expression for the difference in barrier energy given in [EQN 006]. This difference is positive for all values of ($0 \leq \theta < \pi$) corresponding to film-substrate systems that meet the dewetting precondition, and indicates that the presence of the cap will act to slow or suppress the formation of perturbations.

$$\Delta E_c - \Delta E_u = a_1 \left(\gamma_{sg} - \gamma_{ls} + \gamma_{lg} \right) = a_1 \gamma_{lg} \left(1 + \cos\theta \right) \quad \text{[EQN 006]}$$

9.2 DAMPENING THE INSTABILITY

The viscoelastic relaxation, while initially believed to inhibit void formation by not delaminating from the liquid metal, may play a critical role in dampening the surface instabilities. Each of the dynamic instability mechanisms described in Section 1 tends to further destabilize the liquid surface, yet the optical micrographs in Figure 7, Figure 8, and Figure 10 show no systematic uncovering of the substrate. These optical micrographs show some prominent roughening of the surfaces of the metals, especially for the narrowest illuminations and at the edges of the wider illuminations. When the tendency for wider line irradiations to appear smoother is considered, this surface roughening may be related to edge effects imposed by limitations of the projection illumination system, and not fundamental instability mechanisms. Comparisons of similar illumination conditions (line width and fluence) are unfortunately inconclusive.

The centerline portions of ~30 μm line irradiations of Au, Cu, and Ni show a relatively flat topography. (Observations on the centerline topography for the Cr system are difficult to assess due to the tearing during cooling.) We have no atomic force microscopy scans nor profilometry data to quantify the degree of roughening of the upper and lower surfaces of the solidified metal, but the underlying thermal SiO_2 is assumed to roughen only slightly in comparison to the capping oxide. The optical microscopy, when run in differential interference contrast mode, should give qualitative information regarding the top surface of the metal film. For the Au and Cu films, the capping SiO_2 layer shows some bowing near the edges of the line illuminations, but no bowing or other identifiable feature is observable at the centerline. For the Ni films, where the capping oxide is not damaged or cracked, the centerline has a uniform mottled appearance. These

spots are small enough that they are near the resolution limit of the microscope and remain unidentified.

10.0 CONCLUSIONS

10.1 SUBSTRATE CLEANING

Substrate cleaning techniques should be expected to factor in to the analysis of dewetting events. Surprisingly, the consecutive rinsing with acetone, isopropanol, and DI water was found sufficient. Additional tests using RCA cleaning or hydrofluoric acid etching before metal film deposition showed no significant differences in metal film adhesion or behavior during laser melting. This equivalence allowed the use of more benign chemicals during the substrate cleaning, significantly simplifying substrate cleaning procedures. These similar behaviors indicate an inherent robustness to substrate heterogeneities in the sample layer configuration, although careful sample preparation—typically in clean rooms—cannot be ruled out.

10.2 CAPPING OXIDE EFFECTS

The current experiments indicate that Ni, Au, Cu, and Cr films that normally dewet upon laser melting remain continuous when capped with a 500+ nm SiO_2 thick film. Although these observations do not reveal which specific dewetting processes are active or dominant, it is clear that the presence of capping layer is suppressing or slowing the mechanisms associated with dewetting as observed in uncapped films. The 500+ nm thick SiO_2 layer was found to be adequate to maintain mechanical integrity and sufficiently control most dewetting events during laser melting.

Where dewetting could be suppressed, the maximum usable fluences were limited primarily by a complex array of oxide failures. Failure modes vary across the irradiated line widths, but common failure modes were cracking of the oxide layer, bowing of the oxide along the

centerline and edges, and delamination of the oxide outside the irradiated area. These failure modes are believed to be associated with thermal and mechanical stresses. With increased layer thickness, the mechanical integrity of the oxide was maintained. Dewetting, when it occurred, appeared to be associated with cracks, pores, or holes in the oxide that allow atmospheric gases to enter and affect the surface energy balance in the system. In some cases, it was observed that molten metal solidified into a peak-like structure that rose above the oxide. The origin of these structures is unclear and could be a result of liquid metal having up welled into an existing pore.

As noted above and elsewhere [28], the addition of the a capping overlayer beneficially changes the balance of surface free energies so as to increase the barrier energy for nucleation and growth of holes in the liquid metal film, which are believed to initiate dewetting.

To effectively suppress dewetting in laser melted metal films, the capping oxide should conform to specific criteria:

1. Optical feasibility
2. Inertness
3. No outgassing
4. Structurally sound
5. Layer strength
6. Viscoelastic response

1. *Optical feasibility.* For the underlying material to be directly melted via laser irradiation, the capping layer must be transparent to the incident laser wavelength. There is an early report [18] of laser melting that used a CO_2 infrared laser to melt SiO_2 encapsulated Si *indirectly*. This report capitalized on optical transparency of the underlying Si wafer and the relative opaqueness of the SiO_2 to act as an *indirect* heat source, but this type of experiment is relatively rare.

2. *Inertness.* The capping layer should be chemically non-interacting with the metal, both in the solid and liquid phases, thereby avoiding potential compound formation, including but not

limited to metal oxidation. No other appreciable degradation should occur in the temperature range relevant to the metal melting temperature.

3. *No outgassing.* The capping layer should not release gas-phase impurities or dissociate into volatile components upon laser processing as the presence of gases can potentially lower the barrier energy for hole nucleation and growth in the molten metal film. This may require modifications to standard deposition parameters and/or the addition of an appropriate anneal to degas the capping layer before laser irradiation.

4. *Gas barrier.* The capping layer should be free from preexisting cracks and/or pores that could allow atmospheric gases to enter the layer stack and thereby instigate dewetting. In addition, the capping layer should not become porous during the laser irradiation and melt duration of the metal. These flaws can locally negate the benefits of the capping layer.

5. *Layer integrity.* The capping layer should tolerate the mechanical stresses during melting and solidification of the metal film. The capping layer should not crack, shatter, or balloon during the pressure transients associated with volumetric changes during melting and solidification. Strictly, the capping layer should maintain integrity until after the resolidification process is complete.

6. *Viscoelastic response.* New research by Huang et. al. [17] on solid-on-liquid films, a variant of encapsulation, has revealed that the viscoelastic dampening effect of the solid capping layer plays a large role in suppressing the longest wavelength oscillations.

While the extent and thresholds of the processing maps were expected to depend on many factors, these four metal systems have shown common trends. The processing window for suppression of dewetting has been found only in a fluence band above the complete melting threshold, and then only when the capping oxide retained both mechanical integrity and

continuous coverage during the melting process. A second similarity was that the capping oxide appeared to have more mechanical integrity at narrower line irradiations and less so at larger line irradiations. These common trends have been incorporated into a generalized process map as depicted in Figure 12.

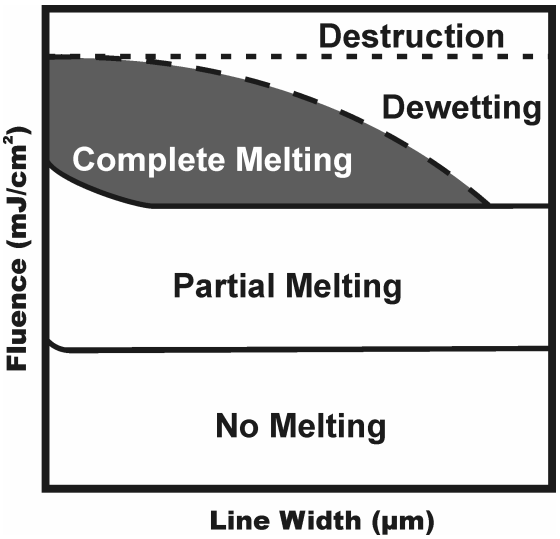

Figure 12: Assumed form for processing window for Au, Ni, Cu, and Cr in these experiments.

This processing map may apply generally to pulsed laser melting of encapsulated thin films. The upper boundary of the process window need not have a specific form and is a complex function of many variables and can vary as a function of the projected line width. In our studies, the upper limit is primarily the onset of dewetting events of some form, although some form of oxide damage cannot be ruled out as the limiting case. For the dewetting mediated region of the processing window, the upper limit is expected to coincide with the complete melting threshold at some line width, thereby excluding any prospects of possible processing with suppressed dewetting for all line widths larger than this line width value. This maximum processing line width will differ for each system.

BIBLIOGRAPHY

[1] K. Jain. *Excimer Laser Lithography.* SPIE Optical Engineering Press, Bellingham, WA.1990.

[2] V. Schultze and A. Fisher. Thin Solid Films, 182 (1989) 23-33

[3] A.T. Voutsas. Appl. Surf. Sci., 208-209 (2003) 250-262.

[4] H.J. Kim and J.S. Im. Appl. Phys. Lett., 68 (1996) 1513-1515.

[5] A. Sharma. Eur. Phys. J. E Soft Matter, E12 (2003) 397-408.

[6] U. Thiele. Eur. Phys. J. E Soft Matter, E12 (2003) 409-416.

[7] S. Herminghaus. J. Phys.: Condens. Matter, 17 (2005) S261-S264. The entire issue is devoted to wetting, where Herminghaus served as the guest editor.

[8] D.J. Srolovitz and M.G. Goldiner. J. Metals, 3 (1995) 31-35, 76-77.

[9] J. Bischof, D. Scherer, S. Herminghaus, and P. Leiderer. Phys. Rev. Lett., 77 (1996) 1536-1539.

[10] S. Herminghaus, K. Jacobs, K. Mecke, J. Bischof, A. Fery, M. Ibn-Elhaj, and S. Schlagowski. Science, 282 (1998) 916-919.

[11] R. Seemann, S. Herminghaus, C. Neto, S. Schlagowski, D. Podzimek, R. Konrad, H. Mantz, and K. Jacobs. J. Phys.: Condens. Matter, 17 (2005) S261-S267-S290

[12] G. Callegari, A. Calvo, J.-P. Hulin, and F. Brochard-Wyart. Langmuir, 18 (2002) 4795-4798.

[13] O. Bostanjoglo and T. Nink. J. Appl. Phys., 79, 11 (1996) 8725-8729.

[14] V.S. Ajaev and D.A. Willis. Phys. Fluids., 15, 10 (2003) 3144-3150.

[15] I. Ursu, I.N. Mihailescu, A. Popa, A.M. Prokhorov, V.P. Ageev, A.A. Gorbunov, and V.I. Konov. J. Appl. Phys., 58 (1985) 3909-3913.

[16] A.E. Siegman and P.M. Fauchet. IEEE J. Quant. Elec., QE-22, 8 (1996) 1384-1403.

[17] R. Huang and Z. Suo. Thin Solid Films, 429 (2003) 273-281.

[18] E. Yablonovitch and T. Gmitter. J. Electrochem. Soc.: Solid-state Sci. & Tech., 131, No. 11 (1984) 2625-2630.

[19] C. Wang, G. Krausch, and M. Geoghegan. Langmuir, 17 (2001) 6269-6274.

[20] P. Müller-Buschbaum. Eur. Phys. J. E., 12 (2003) 443-448.

[21] J.P. Leonard, M.A. Bessette, V.V. Gupta, and J.S. Im. Mat. Res. Soc. Symp. Proc., 452 (1997) 947-952.

[22] J. Becker, G. Grün, R. Seemann, H. Mantz, K. Jacobs, K.R. Mecke, and R. Blossy. Nature Materials, 2 (2002) 59-63.

[23] V.V. Gupta, H.J. Song and J.S. Im. Mat. Res. Soc. Symp. Proc., 452 (1997) 941-946.

[24] G. Carbone and B.N.J. Persson. J. Chem. Phys., 121 (2004) 2246-2252.

[25] J.E. Kline and J.P. Leonard. "Suppression of dewetting during excimer laser melting of thin metal films on SiO_2." In press, Thin Solid Films (2005).

[26] C. Hill and D.J. Godfrey. J. Phys. Colloq., 41, C4 (1980) 79-84.

[27] G.E. Jellison, D.H. Lowndes, and J.W. Sharp. J. Mater. Res., 3 (1988) 498-505.

[28] J.E. Kline and J.P. Leonard. "Suppression of Dewetting in Pulsed Laser Melting of Thin Metallic Films on SiO_2" in *Stability of Thin Films and Nanostructures*, edited by R.P. Vinci, R. Schwaiger, A. Karim, and V. Shenoy (Mater. Res. Soc. Symp. Proc. 854E, Warrendale, PA, 2005), U11.6.